Jointly Segmenting Prostate Zones in 3D MRIs by Globally Optimized Coupled Level-Sets

Jing Yuan[1], Eranga Ukwatta[1], Wu Qiu[1], Martin Rajchl[1], Yue Sun[1], Xue-Cheng Tai[2], and Aaron Fenster[1]

[1] Medical Imaging Labs, Robarts Research Institute,
University of Western Ontario,
London, Ontario, Canada N6A 5K8
{jyuan,eukwatta,wqiu,mrajchl,ysun,afenster}@robarts.ca
[2] Mathematics Department, University of Bergen,
Bergen, Norway
tai@math.uib.no

Abstract. It is of great interest in image-guided prostate interventions and diagnosis of prostate cancer to accurately and efficiently delineate the boundaries of prostate, especially its two clinically meaningful sub-regions/zones of the central gland (CZ) and the peripheral zone (PZ), in the given magnetic resonance (MR) images. We propose a novel coupled level-sets/contours evolution approach to simultaneously locating the prostate region and its two sub-regions, which properly introduces the recently developed convex relaxation technique to jointly evolve two coupled level-sets in a global optimization manner. Especially, in contrast to the classical level-set methods, we demonstrate that the two coupled level-sets can be simultaneously moved to their globally optimal positions at each discrete time-frame while preserving the spatial inter-surface consistency; we study the resulting complicated combinatorial optimization problem at each discrete time evolution by means of convex relaxation and show its global and exact optimality, for which we introduce the novel coupled continuous max-flow model and demonstrate its duality to the investigated convex relaxed optimization problem with the region constraint. The proposed coupled continuous max-flow model naturally leads to a new and efficient algorithm, which enjoys great advantages in numerics and can be readily implemented on GPUs. Experiments over 10 T2-weighted 3D prostate MRIs, by inter- and intra-operator variability, demonstrate the promising performance of the proposed approach.

Keywords: Convex Optimization, 3D Prostate Zonal Segmentation.

1 Introduction

Prostate cancer is one of major health problems in the western world, with one in six men affected during their lifetime [1]. In diagnosing prostate cancer, transrectal ultrasound (TRUS) guided biopsies have become the gold standard. However, the accuracy of the TRUS guided biopsy relies on and is limited by

A. Heyden et al. (Eds.): EMMCVPR 2013, LNCS 8081, pp. 12–25, 2013.

the fidelity. Magnetic resonance (MR) imaging is an attractive option for guiding and monitoring such interventions due to its superior visualization of not only the prostate, but also its substructure and surrounding tissues [2, 3]. The fusion of 3D TRUS and MRI provides an effective way to target biopsy needles in the 3D TRUS image toward the prostate region containing MR identified suspicious lesions, which is regarded as an alternative to the more expensive and inefficient MRI-based prostate biopsy [4] and the less accurate conventional 2D TRUS-guieded prostate biopsy. On the other hand, during guidance of the biopsy, the prostate region is usually recognized by two visually meaningful subregions in a prostate MRI: the *central gland* (CG) and the *peripheral zone* (PZ) [5], and up to 80% of prostate cancers are located within the PZ region [6]. The ability to superimpose the 3D TRUS image used to guide the biopsy onto these pre-segmented prostate zones(subregions) of interest in MRIs is highly desired in a fused 3D TRUS/MRI guided biopsy system. In addition, computer aided diagnosis (CAD) techniques for prostate cancer can also benefit from the correct interpretation of the prostate zonal anatomy since the occurrence and appearance of the cancer depends on its zonal location [7, 8]; and the ratio of CG volume to whole prostate gland (WG) can be used to monitor prostate hyperplasia [9]. To this end, efficient and accurate extraction of the prostate region, in particular its sub-regions of CG and PZ, from 3D prostate MRIs is of great interest in both image-guided prostate interventions and diagnosis of prostate cancer.

Many studies focused their efforts on the segmentation of the whole prostate in 3D MR images (especially in T2w 3D MRIs), see [10] for a review; where the obvious intensity inhomogeneity of prostate makes the segmentation task challenging. However, only few studies focused on the segmentation of the prostate sub-regions/zones in 3D MRIs. Allen *et al.* [11] proposed a method for the automatic delineation of the prostate boundaries and CG, which was limited to the middle region of the prostate (where T2w contrast permits accurate segmentation), and ignored the apex and base of the gland. Yin *et al.* [12] proposed an automated CG segmentation algorithm based on Layered Optimal Graph Image Segmentation of Multiple Objects and Surfaces (LOGISMOS). The first paper about segmenting the prostate into two regions of PZ and CG was proposed by Makni *et al.* [13]. The authors proposed a modified version of the evidential C-means algorithm to cluster voxels into their respective zones incorporating the spatial relation between voxels in 3D multispectral MRIs including a T2w image, a diffusion weighted image (DWI), and a contrast enhanced MRI (CEMRI). More recently, Litjens *et al.* [14] proposed a pattern recognition method to classify the voxels using anatomical, intensity and texture features in multispectral MRIs. However, in [13] and [14], the segmentation of prostate peripheral zone relies on the manual segmentation of the whole prostate gland.

Contributions: Based on recent developments of the new global optimization technique to the single level-set/contour propagation [15–17], we propose a new global optimization-based coupled level-set evolution approach to delineating the whole prostate gland (WG) and its subregions of CG and PZ jointly from a

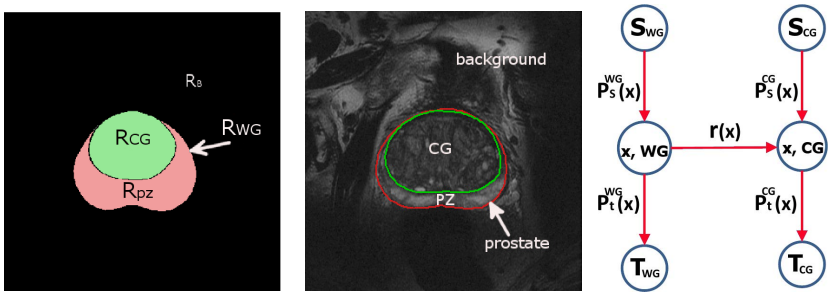

(a) (b) (c)

Fig. 1. (a) shows the proposed layout of anatomically consistent regions: the whole prostate(WG) $\mathcal{R}_{WG}$ and its two zones: central gland(CG) $\mathcal{R}_{CG}$ and peripheral zone(PZ) $\mathcal{R}_{PZ}$, which are mutually distinct from the background region R_B. (b) illustrates the segmented contours overlaid on a T2w prostate MRI slice.

single input 3D T2 weighted prostate MR image. The proposed method matches the intensity distribution models of the two prostate sub-regions CG and PZ to guide the simultaneous propagation of two coupled level-sets. We efficiently and globally solve the resulted challenging combinatorial optimization problem, the so-called *coupled min-cut model*, during each discrete time evolution by means of convex relaxation. We propose a novel spatially continuous flow-maximization model, i.e. the *coupled continuous max-flow model*, and demonstrate its duality to the studied convex relaxed optimization problem with the region consistency constraint. The *coupled continuous max-flow model* directly leads to a new and efficient *continuous max-flow based* algorithm, which enjoys great advantages in numerics and can be readily implemented on GPUs. Experiments over 10 T2-weighted 3D prostate MRIs, by inter- and intra-operator variability, demonstrate the promising performance of the proposed approach. The proposed method can be easily applied to other image segmentation tasks.

The classical level-set methods [18] are based on locally computing the associated convention PDE in a time-explicit manner and converge slowly; especially, an extremely complex scheme is required for correctly propagating multi-class level-sets. In contrast, the global optimization based contour evolution technique introduces a new implicit-time contour convenction scheme which allows the large time step-size to accelerate convergence, and the inter-level-set contraints can be easily adapted into the propagation process in a global optimization way (as the proposed approach in this work).

2 Global Optimization to Coupled Contour Evolution

Now we target to segment a given 3D T2w prostate MR image $I(x)$ into the prostate region $\mathcal{R}_{WG}$ together with its two mutually distinct sub-regions: the

central gland $\mathcal{R}_{CG}$ and the peripheral zone $\mathcal{R}_{PZ}$, where $\mathcal{R}_B$ denotes the background (see Figure 1(a)), i.e.

$$\Omega \,=\, \mathcal{R}_{WG} \cup \mathcal{R}_B\,, \quad \mathcal{R}_{WG} \cap \mathcal{R}_B \,=\, \emptyset\,, \tag{1}$$

where the two spatially coherent sub-regions: the R_{CG} and R_{PZ} constitute the whole prostate region $\mathcal{R}_{WG}$ such that

$$\mathcal{R}_{WG} \,=\, \mathcal{R}_{CG} \cup \mathcal{R}_{PZ}\,; \quad \mathcal{R}_{CG} \cap \mathcal{R}_{PZ} \,=\, \emptyset\,. \tag{2}$$

In this context, we propose a novel global optimization based approach to jointly evolving two coupled contours $\mathcal{C}^{WG}$ and $\mathcal{C}^{CG}$ to the correct boundaries of the prostate and the central gland, while keeping the inter-contour relationship

$$\mathcal{R}_{CG} \,\subset\, \mathcal{R}_{WG}\,; \tag{3}$$

i.e. the inclusion region $\mathcal{R}_{CG}$ of $\mathcal{C}^{CG}$ is covered by the inclusion region $\mathcal{R}_{WG}$ of $\mathcal{C}^{WG}$. Clearly, once the two contours $\mathcal{C}^{CG}$ and $\mathcal{C}^{WG}$ are computed, the peripheral zone $\mathcal{R}_{PZ}$ is determined by the complementary region $\mathcal{R}_{WG} \backslash \mathcal{R}_{CG}$. We show that the resulting combinatorial optimization at each discrete-time contour propagation can be solved globally and exactly by convex relaxation, which means that the two contours can be moved to their 'best' positions during each discrete time evolution. With this respect, we propose and investigate a unified framework in terms of *coupled continuous max-flow model*. In addition, the new optimization theory can be used to drive an efficient *coupled continuous max-flow* based algorithms, which have great numerical advantages and can be readily implemented on graphics processing units (GPU) to achieve a high computation performance. The proposed optimization theory and algorithm can be directly extended to the general case of evolving $n > 2$ contours $\mathcal{C}^i$, $i = 1 \ldots n$, while preserving the order $\mathcal{C}_t^n \subset \mathcal{C}_t^{n-1} \ldots \subset \mathcal{C}_t^1$; and also applied to other image segmentation applications.

2.1 Matching Multiple Intensity Distribution Models

One major challenge to segment a typical T2w prostate MR image is the strong intensity inhomogeneity of prostate (see Figure 1(a)), where the zones R_{CG} and R_{PZ} of $\mathcal{R}_{WG}$ have their distinct intensity appearances, hence constitute the complex appearance model of the prostate region $\mathcal{R}_{WG}$. In this work, we propose to model the intensity appearance of the prostate region $\mathcal{R}_{WG}$ by the two independent appearance models of its two sub-regions $\mathcal{R}_{CG}$ and $\mathcal{R}_{PZ}$, which are distinct to each other. This sets up a proper composite appearance description of the entire prostate region $\mathcal{R}_{WG}$ in practice. Such a composite intensity appearance model is shown to be more accurate than the often-used mixture appearance model in practice [19]. Indeed, the two separated appearance models can be obtained much easier and more accurately, with less influence by sampling statistics, than the direct mixture appearence model of $\mathcal{R}_{WG}$. We propose to match the two distinct appearance models of the prostate sub-regions R_{CG} and R_{PZ} in stead of the mixture model of the prostate $\mathcal{R}_{WG}$.

Let $\pi_i(z)$, $i \in \{CG, PZ\}$, be the intensity probability density function (PDF) of the respective prostate sub-region $\mathcal{R}_i$ and $z \in \mathcal{Z}$ gives the photometric value of intensities. Also, let $\pi_B(I(x))$ be the PDF of the background region $\mathcal{R}_B$. In practice, such PDFs of intensities of the interesting object regions provide a reliable and global description of the segmented objects [20], which can be learned from either sampled pixels or given training datasets.

Given the indicator functions $u_i(x) \in \{0, 1\}$, $i \in \{CG, WG\}$, of the inclusion region of the contour $\mathcal{C}^i$:

$$u_i(x) := \begin{cases} 1\,, \text{where } x \text{ is inside } \mathcal{C}^i \\ 0\,, \text{otherwise} \end{cases}, \quad i \in \{CG, WG\}\,, \tag{4}$$

the Bhattacharyya distance [20] is used for matching the PDFs of the three distinct regions: $\mathcal{R}_{CG}$, $\mathcal{R}_{PZ}$ and $\mathcal{R}_B$; which results in the following model-matching term:

$$E_m(u) = -\sum_{z \in \mathcal{Z}} \left\{ \sqrt{\pi_{CG}(z)\,\phi_{CG}(z)} + \sqrt{\pi_{PZ}(z)\,\phi_{PZ}(z)} + \sqrt{\pi_B(z)\,\phi_B(z)} \right\} \tag{5}$$

where $\phi_{CG,PZ,B}(u, z)$ are the respective PDFs for the estimated regions of $\mathcal{R}_{CG}$, $\mathcal{R}_{PZ}$ and $\mathcal{R}_B$, and computed by the Parzen method:

$$\phi_{CG}(z) = \frac{\int_\Omega K(z - I(x))\, u_{CG}\, dx}{\int u_{CG}\, dx}\,, \quad \phi_{PZ}(z) = \frac{\int_\Omega K(z - I(x))\, (u_{WG} - u_{CG})\, dx}{\int (u_{WG} - u_{CG})\, dx}$$

and

$$\phi_B(z) \;=\; \frac{\int_\Omega K(z - I(x))\, (1 - u_{WG})\, dx}{\int (1 - u_{WG})\, dx}$$

where $K(\cdot)$ is the Gaussian kernel function $K(x) = \frac{1}{\sqrt{2\pi\sigma^2}} \exp(-x^2/2\sigma^2)$.

Optimization Model: In view of the histogram matching energy function (5) and region constraint (3), we propose to compute the region indictor functions $u_{CG}(x), u_{WG}(x) \in \{0, 1\}$ by minimizing the following energy function

$$\min_{u_{CG}, u_{WG}(x) \in \{0,1\}} E_m(u) \;+\; \int_\Omega g(x)\, |\nabla u_{CG}(x)|\; dx \;+\; \int_\Omega g(x)\, |\nabla u_{WG}(x)|\; dx \tag{6}$$

subject to the inter-region constraint

$$u_{CG}(x) \;\leq\; u_{WG}(x)\,, \quad \forall x \;\in\; \Omega\,; \tag{7}$$

where the total-variation functions properly approximates the weighted areas of $\mathcal{R}_{CG}$ and $\mathcal{R}_{WG}$ and (7) corresponds to (3).

2.2 Global Optimization and Coupled Contour Evolution

Now we study the optimization problem (6) and introduce a novel global optimization based approach to evolving the two contours $\mathcal{C}^{CG}$ and $\mathcal{C}^{WG}$, w.r.t. $\mathcal{R}_{CG}$ and $\mathcal{R}_{WG}$, simultaneously while preserving the constraint (3).

Single Contour Evolution and Min-Cut: In contrast to the classical level-set evolution theory, the recent developments [16, 17] of the global optimization theory to the evolution of a single contour $\mathcal{C}$ proves that the propagation of the contour $\mathcal{C}_t$ at time t to its new position $\mathcal{C}_{t+h}$ at time $t+h$ can be modeled and globally optimized in terms of computing the *min-cut* problem:

$$\mathcal{C}_{t+h} \;:=\; \min_{\mathcal{C}} \int_{\mathcal{C}^+} c^+(x)\,dx \;+\; \int_{\mathcal{C}^-} c^-(x)\,dx \;+\; \int_{\partial\mathcal{C}} g(s)\,ds\,, \tag{8}$$

where

1. $\mathcal{C}^+$ indicates the region expansion w.r.t. $\mathcal{C}_t$: for $\forall x \in \mathcal{C}^+$, it is initially outside $\mathcal{C}_t$ at time t, and 'jumps' to be inside $\mathcal{C}_{t+h}$ at $t+h$; for such a 'jump', it pays the cost:
$$c^+(x) = \big(\mathrm{dist}(x, \partial\mathcal{C}_t) + f(x)\big)/h\,; \tag{9}$$
2. $\mathcal{C}^-$ indicates the region shrinkage w.r.t. $\mathcal{C}_t$: for $\forall x \in \mathcal{C}^-$, it is initially inside $\mathcal{C}_t$ at t, and 'jumps' to be outside $\mathcal{C}_{t+h}$ at $t+h$; for such a 'jump', it pays the cost $c^-(x)$:
$$c^-(x) = \big(\mathrm{dist}(x, \partial\mathcal{C}_t) - f(x)\big)/h\,. \tag{10}$$

The function $\mathrm{dist}(x, \partial\mathcal{C}_t)$ gives the distance of any $x \in \Omega$ to the current contour $\mathcal{C}_t$, where Ω is the image domain; the outer force function $f(x)$ is data-associated and is chosen based on the specified application: for example, $f(x)$ can be defined using the first-order variation of the distribution matching function, e.g. the Bhattacharyya distance. Obviously, the time step-size h is implicitly adapted in the cost functions (9)-(10), which allows a large value in numerical practice to speed-up the evolution of contours towards convergence.

To be more clear, we define the cost functions $D_s(x)$ and $D_t(x)$ as follows:

$$D_s(x) \;:=\; \begin{cases} c^-(x)\,, & \text{where } x \in \mathcal{C}_t \\ 0\,, & \text{otherwise} \end{cases}\,, \quad D_t(x) \;:=\; \begin{cases} c^+(x)\,, & \text{where } x \notin \mathcal{C}_t \\ 0\,, & \text{otherwise} \end{cases}\;; \tag{11}$$

which can be interpreted as the cost of assigning each pixel x to be foreground or background, respectively. Let $u(x) \in \{0, 1\}$ be the labeling function of the new contour $\mathcal{C}$ in (8). Therefore, the proposed optimization model (8) to contour evolution can be equally reformulated as the *min-cut model*:

$$\min_{u(x)\in\{0,1\}} \; \langle 1-u, D_s\rangle + \langle u, D_t\rangle + \int_{\Omega} g(x)\,|\nabla u|\;dx\,, \tag{12}$$

which can be solved globally and exactly with various efficient algorithms of graph-cut and convex optimization!

Coupled Contour Evolution and Coupled Min-Cuts: Following the same ideas of (8), for the evolution of the contour $\mathcal{C}^{CG}$ during the discrete time-frame from t to $t+h$, we, correspondingly, define the cost functions $c^+_{CG}(x)$ and $c^-_{CG}(x)$ w.r.t. region expansion $\mathcal{C}^+_{CG}$ and shrinkage $\mathcal{C}^-_{CG}$; for the evolution of $\mathcal{C}^{WG}$, we

define $c^+_{WG}(x)$ and $c^-_{WG}(x)$ as the respective costs to region changes. Therefore, we optimize the problem (6) by evolving the two contours $\mathcal{C}^{CG}$ and $\mathcal{C}^{WG}$, which propagates the contours $\mathcal{C}^{CG}_t$ and $\mathcal{C}^{WG}_t$ at time t to their new positions $\mathcal{C}^{CG}_{t+h}$ and $\mathcal{C}^{WG}_{t+h}$ while preserving the constraint (3): $\mathcal{R}_{CG} \subset \mathcal{R}_{WG}$ by the following minimization problem:

$$\min_{\mathcal{C}^{CG},\mathcal{C}^{WG}} \sum_{i\in\{CG,WG\}} \Big\{ \int_{\mathcal{C}^+_i} c^+_i(x) \, + \int_{\mathcal{C}^-_i} c^-_i(x) \, + \int_{\partial\mathcal{C}^i} g(s) \Big\} \tag{13}$$

subject to the region constraint $\mathcal{R}_{CG} \subset \mathcal{R}_{WG}$.

Similar as (11), we define the label assignment cost functions $D^i_s(x)$ and $D^i_t(x)$, $i \in \{CG, WG\}$, such that:

$$D^i_s(x) := \begin{cases} c^-_i(x)\,, \text{ where } x \in \mathcal{C}^i_t \\ 0\,, \qquad \text{otherwise} \end{cases}, \quad D^i_t(x) := \begin{cases} c^+_i(x)\,, \text{ where } x \notin \mathcal{C}^i_t \\ 0\,, \qquad \text{otherwise} \end{cases}. \tag{14}$$

In consequence, the optimization problem (13) can be equally represented by

$$\min_{u_{CG,WG}(x)\in\{0,1\}} \sum_{i\in\{CG,WG\}} \Big\{ \langle 1-u_i, D^i_s\rangle + \langle u_i, D^i_t\rangle + \int_\Omega g\,|\nabla u_i|\; dx \Big\} \tag{15}$$

subject to the linear inequality region constraint (7), i.e. $u_{CG}(x) \leq u_{WG}(x)$.

Clearly, without the constraint (7), the formulation (15) gives rise to two independent min-cut problems; the region constraint (7) conjoins these two independent min-cut problems with each other. Hence, in this paper, we call (15) the model of *coupled min-cuts* in the spatially continuous setting, i.e. the *coupled continuous min-cut model*.

Convex Relaxation and Coupled Continuous Max-Flow Model: In this work, we investigate the proposed challenging combinatorial optimization problems (15) by convex relaxation, where the binary constrained labeling functions $u_{CG,WG}(x) \in \{0, 1\}$ are relaxed to be the convex constraint $u_{CG,WG}(x) \in [0, 1]$. Therefore, we have the corresponding convex relaxation problem:

$$\min_{u_{CG,WG}\in[0,1]} \sum_{i\in\{CG,WG\}} \Big\{ \langle 1-u_i, D^i_s\rangle + \langle u_i, D^i_t\rangle + \int_\Omega g\,|\nabla u_i|\; dx \Big\}, \tag{16}$$

subject to the region constraint (7).

In the following sections, we propose the novel dual model to the convex optimization problem (16), which corresponds to maximize the streaming flows upon a novel coupled flow-maximization setting, i.e. the *coupled continuous max-flow model*. With help of the new *coupled continuous max-flow model*, we show the convex relaxed optimization problem (16) solves the original combinatorial optimization (16) exactly and globally! This means the two coupled contours $\mathcal{C}^{CG}$ and $\mathcal{C}^{WG}$ can be moved to their globally optimized positions, i.e. best positions, during each discrete time frame. In addition, we can directly derive the new *coupled continuous max-flow algorithm* which avoids tackling the non-smooth function terms and linear constraint in (16) and enjoys a fast convergence.

Coupled Continuous Max-Flow Model: To motivate the *coupled continuous max-flow model*, we introduce a novel flow configuration (shown in Fig. 1(c)), which is the combination of two independent standard flow-maximization settings (see [21, 22] etc.), linked by an additional directed flow $r(x)$ in-between:

- We set up two copies Ω_{CG} and Ω_{WG} of Ω w.r.t. the essential two continuous min-cuts; for Ω_i, $i \in \{CG, WG\}$, two extra nodes s_i and t_i are added as the source and sink terminals; we link s_i to each pixel $x \in \Omega_i$ and link x to t_i, see Fig. 1(c); moreover, within each of Ω_i, $i \in \{CG, WG\}$, we define the source flow $p_s^i(x)$ which is directed from s_i to each x and the sink flow $p_t^i(x)$ which is directed from each x to t_i; also, within each of Ω_i, there is the spatial flow $q^i(x)$ around each pixel x.
- At each pixel x, there exists an extra flow $r(x)$ directed from Ω_2 to Ω_1.

For the two source flow fields $p_s^{CG}(x)$ and $p_s^{WG}(x)$, we define the flow capacity constraints:

$$p_s^{CG}(x) \,\leq\, D_s^{CG}(x)\,, \quad p_s^{WG}(x) \,\leq\, D_s^{WG}(x)\,; \quad \forall x \,\in\, \Omega\,. \tag{17}$$

Likewise, for the two sink flow fields: $p_t^{CG}(x)$ and $p_t^{WG}(x)$, and the spatial flows: $q^{CG}(x)$ and $q^{WG}(x)$, we define the respective flow capacity constraints:

$$p_t^{CG}(x) \,\leq\, D_t^{CG}(x)\,, \quad p_t^{WG}(x) \,\leq\, D_t^{WG}(x)\,; \quad \forall x \,\in\, \Omega\,; \tag{18}$$

and

$$\left|q^{CG}(x)\right| \,\leq\, g(x)\,, \quad \left|q^{WG}(x)\right| \,\leq\, g(x)\,; \quad \forall x \,\in\, \Omega\,. \tag{19}$$

Moreover, the extra directed flow field $r(x)$ for each x at Ω_{WG} to the same position at Ω_{CG} is constrained by

$$r(x) \,\geq\, 0\,; \quad \forall x \,\in\, \Omega\,. \tag{20}$$

In addition to the above flow capacity constraints, at each pixel $x \in \Omega_i$, $i \in \{CG, WG\}$, all the flow fields $p_s^i(x)$, $p_t^i(x)$, $q_i(x)$ and $r(x)$ are balanced such that

$$R_{CG}(x) \,:=\, \mathrm{div}\, q^{CG}(x) \,+\, p_t^{CG}(x) \,-\, p_s^{CG}(x) \,-\, r(x) \,=\, 0\,; \tag{21}$$

and

$$R_{WG}(x) \,:=\, \mathrm{div}\, q^{WG}(x) \,+\, p_t^{WG}(x) \,-\, p_s^{WG}(x) \,+\, r(x) \,=\, 0\,. \tag{22}$$

Therefore, we propose the novel *coupled continuous max-flow model* which achieves the maximum total flows directed from s_1 and s_2, i.e.

$$\max_{p_s, p_t, q, r} \int_\Omega p_s^{CG}\, dx \,+\, \int_\Omega p_s^{WG}\, dx \tag{23}$$

subject to the flow capacity conditions (17) - (20) and the flow conservation conditions (21) and (22).

Duality and Global Optimum to (15)**:** Note that (23) provides two independent continuous max-flow problems, which are linked by the extra directed flow field $r(x)$. We can prove the duality between the *coupled continuous max-flow model* (23) and the convex relaxed optimization problem (16), (see [22, 23])

Proposition 1. *The proposed* coupled continuous max-flow model (23) *is equivalent or dual to the convex relaxed coupled continuous min-cut formulation* (16)*:*

$$(23) \iff (16)\,.$$

Clearly, for the given convex relaxation problem (16), the global optimum exists. In addition, with helps of the proposed continuous max-flow model (23), we can prove thresholding the global optimum of (16) also solve the original combinatorial optimization problem (15). This means that the two contours $\mathcal{C}^{CG}$ and $\mathcal{C}^{WG}$ can be moved to their 'best' position(s), i.e. the global optimum, during each discrete time frame!

Proposition 2. *Let* $u^*_{CG}(x), u^*_{WG}(x) \in [0,1]$ *be any global optimum of the convex relaxed coupled continuous min-cut formulation* (16)*, their thresholds* $u^\ell_{CG}(x) \in \{0,1\}$ *and* $u^\ell_{WG}(x) \in \{0,1\}$*:*

$$u^\ell_i(x) \;=\; \begin{cases} 1\,, & \textit{when } u^*_i(x) > \ell \\ 0\,, & \textit{when } u^*_i(x) \le \ell \end{cases}\,, \quad i \in \{CG, WG\} \tag{24}$$

for any $\ell \in [0,1)$*, solves the original binary-constrained coupled continuous min-cut problem* (15) *globally and exactly.*

Actually, the functions $u^\ell_{CG}(x), u^\ell_{WG}(x) \in \{0,1\}$ *indicate the new positions of the two thresholded level-sets* $\mathcal{C}^{CG}$ *and* $\mathcal{C}^{WG}$ *respectively, which are the globally optimized contours to* (13)*.*

The proofs of Prop. 1 and Prop. 2 are omitted here due to the limit space.

Coupled Continuous Max-Flow Algorithm: On the other hand, the proposed *coupled continuous max-flow model* (23) naturally leads to an efficient *coupled continuous max-flow based algorithm* in a multiplier-augmented way [24] (similar as [22, 23]). Based on the augmented Lagrangian algorithmic scheme, we introduce the multiplier functions $u_{CG}(x)$ and $u_{WG}(x)$ to (21) and (22) respectively and define the Lagrangian function:

$$L(p_s, p_t, q, r, u) := \int_\Omega p^{CG}_s(x)\,dx + \langle u_{CG}, R_{CG}\rangle + \int_\Omega p^{WG}_s(x)\,dx + \langle u_{WG}, R_{WG}\rangle\,.$$

We also define the following augmented Lagrangian function

$$L_c(p_s, p_t, q, r, u) := L(p_s, p_t, q, r, u) - \frac{c}{2}\,\|R_{CG}\|^2 - \frac{c}{2}\,\|R_{WG}\|^2$$

where $c > 0$ is constant.

We proposed the *coupled continuous max-flow algorithm* which explores the following iteration till convergence: each k-th iteration consists of the flow maximization steps over the flow functions p_s, p_t, q and r and corresponding flow constraints, and the label updating steps:

1. Maximize $L_c(p_s, p_t, q, r, u)$ over the spatial flows $\left|q^i(x)\right| \leq g(x)$, $i \in \{CG, WG\}$, by fixing the other variables, which gives

$$(q^i)^{k+1} := \underset{|q^i(x)|\leq g(x)}{\arg\max} -\frac{c}{2}\left\|\operatorname{div} q^i - F_i^k\right\|^2,$$

where

$$F_i^k(x) = \left((p_s^i)^k - (p_t^i)^k - r^k + (u_i)^k\right)(x)/c\,.$$

It can be implemented by the one-step of gradient-projection procedure [25].

2. Maximize $L_c(p_s, p_t, q, r, u)$ over the source flows $p_s^i(x) \leq D_s^i(x)$, $i \in \{CG, WG\}$, by fixing the other variables, which gives

$$(p_s^i)^{k+1} := \underset{p_s^i(x)\leq D_s^i(x)}{\arg\max} \int_\Omega p_s^i\,dx - \frac{c}{2}\left\|p_s^i - G_i^k\right\|^2,$$

where

$$G_i^k(x) = \left(\operatorname{div} q_i^{k+1} + (p_t^i)^k + r^k - (u_i)^k/c\right)(x)\,.$$

It can be solved exactly by:

$$(p_s^i)^{k+1}(x) \;=\; \min\left(G_i^k(x) + 1/c\,,\; D_s^i(x)\right). \tag{25}$$

3. Maximize $L_c(p_s, p_t, q, r, u)$ over the sink flows $p_t^i(x) \leq D_t^i(x)$, $i \in \{CG, WG\}$, by fixing the other variables, which gives

$$(p_t^i)^{k+1} := \underset{p_t^i(x)\leq D_t^i(x)}{\arg\max} -\frac{c}{2}\left\|p_t^i + H_i^k\right\|^2,$$

where

$$H_i^k(x) = \left(\operatorname{div} q_i^{k+1} - (p_s^i)^{k+1} + r^k - (u_i)^k/c\right)(x)\,.$$

It can be solved exactly by:

$$(p_t^i)^{k+1}(x) \;=\; \min\left(-H_i^k(x)\,,\; D_t^i(x)\right). \tag{26}$$

4. Maximize $L_c(p_s, p_t, q, r, u)$ over the coupled flow field $r(x) \geq 0$ by fixing the other variables, which gives

$$r^{k+1} := \underset{r(x)\geq 0}{\arg\max} -\frac{c}{2}\left\|r - J_{CG}^k\right\|^2 - \frac{c}{2}\left\|r + J_{WG}^k\right\|^2,$$

where $J_i(x)$, $i \in \{CG, WG\}$, are fixed. It can be compted exactly by

$$r^{k+1}(x) \;=\; \max\left(0, (J_1 - J_2)/2\right).$$

5. Update the multiplier functions $u_i^{k+1}(x)$, $i \in \{CG, WG\}$, by

$$u_i^{k+1}(x) \;=\; u_i^k(x) - c\,R_i^{k+1}(x)\,. \tag{27}$$

The *coupled continuous max-flow* algorithm successfully avoids directly handling the non-smooth functions and linear constraint in the corresponding convex relaxation model (16). The experiments show that the proposed algorithm also obtains a much faster convergence rate in practice. In addition, the *coupled continuous max-flow algorithm* can be readily implemented on GPUs to significantly speed-up computation.

3 Experiments and Results

Experiment Implementation: We applied the proposed continuous max-flow algorithm on 10 T2w MR images acquired using a body coil. Subjects were scanned at 3 Tesla with a GE Excite HD MRI system (Milwaukee, WI, USA). All images were acquired at $512\times512\times36$ voxels with spacing of $0.27\times0.27\times2.2mm^3$. Two closed surfaces were constructed via a thin-plate spline fitting with ten to twelve user selected initial points on the WG and CG surface, respectively, which were used as the initial CG and WG surfaces for surface evolution. The original input 3D image was also cropped by enlarging the bounding box of the initial WG surface by 30 voxels in order to speed up computations. The initial PDFs for the regions of R_{CZ} and R_{PZ} were calculated based on the intensities in the user-initialized CG and PZ regions, respectively.

Evaluation Metrics: The proposed segmentation method was evaluated by comparing the results to manual segmentations in terms of DSC, the mean absolute surface distance (MAD), and the maximum absolute distance (MAXD) [26, 27]. All validation metrics were calculated for the entire prostate gland, central gland and peripheral zone. In addition, the coefficient-of-variation (CV) of DSC [27] was used to evaluate the intra-observer variability of our method introduced by manual initialization.

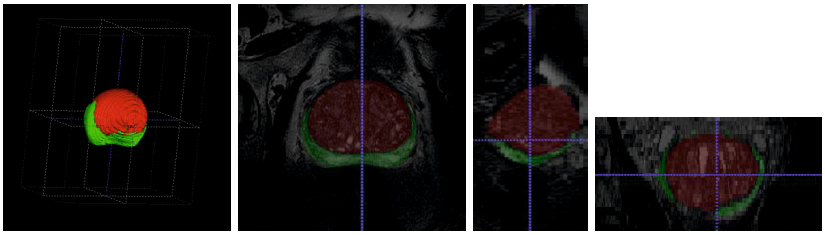

(a) (b) (c) (d)

Fig. 2. Segmentation result of one prostate. (a) rendered resulting surface, (b) axial view, (c) sagittal view, and (d) coronal view, Green: the segmented PZ, red: the segmented CG.

Accuracy: Visual inspections in Fig. 2 show that the PZ and CG regions segmented by the proposed approach agree well with the objects. Quantitative experiment result for 10 patient images using the proposed method is shown in Table 1. The mean DSC was $89.2\pm4.5\%$ for the whole prostate gland, $84.7\pm5.2\%$ for the central gland, and $68.5\pm6.9\%$ for the peripheral zone. In addition, the evaluation results of MAD and MAXD are provided in Table 1, which give similar information to DSC.

Reliablility: Ten images were also segmented three times by the same observer to assess the intra-observer variability introduced by the user initialization. The proposed method initialized by three repetitions yielded a CV of 7.5%, 5.6%, and 5.0% for PZ, CG, and WG, respectively. It can be seen that the proposed

Table 1. Mean segmentation results in terms of DSC, MAD and MAXD for 10 patient images

	DSC (%)	MAD (mm)	MAXD (mm)
PZ	68.5 ± 6.9	4.8 ± 2.1	20.1 ± 11.5
CG	84.7 ± 5.2	3.2 ± 1.2	12.3 ± 3.8
WG	89.2 ± 4.5	2.9 ± 0.9	12.2 ± 4.8

Table 2. Intra-observer variability results in terms of DSC (%) using three repetitions of the same observer for ten patient images

	PZ	CG	WG
experiment 1	68.5 ± 6.9	84.7 ± 5.2	89.2 ± 4.5
experiment 2	67.9 ± 5.8	85.3 ± 4.5	88.7 ± 4.0
experiment 3	69.2 ± 6.5	84.5 ± 4.5	89.0 ± 3.8
CV (%)	7.5	5.6	5.0

method demonstrated low intra-observer segmentation variability for the CG and WG, suggesting a good reproducibility.

Computational Time: The proposed approach was implemented in Matlab (Natick, MA) using CUDA (NVIDIA Corp., Santa Clara, CA). The experiments were performed on a Windows desktop with an Intel i7-2600 CPU (3.4 GHz) and a GPU of NVIDIA Geforce 580X. The mean run time of three repeated segmentations for each 3D MR image was used to estimate the segmentation time in this study. The mean segmentation time was 8 ± 0.5s (converged with 3 - 5 surface evolutions) in addition to 40 ± 5s for initialization, resulting in a total segmentation time of less than $50s$ for each 3D image ($512 \times 512 \times 36$ voxels).

4 Discussions and Conclusions

In this work, we propose and evaluate a new global optimization-based coupled contour evolution approach to simultaneously extracting the boundaries of prostate and its component zones from the input 3D prostate T2w MRI, which address the challenge of segmenting multiple prostate regions in a numerically stable and efficient way. In contrary to the classical level-set methods, the proposed approach demonstrates great advantages in terms of numerical efficiency and moving the coupled contours to their 'best' positions simultaneously while preserving the inter-contour relationship. The introduced algorithm shows reliable performance results with minimal user interactions using ten patient images, suggesting itself for potential clinical use in 3D TRUS/MR image guided prostate interventions and computer aided diagnosis of prostate cancer.

The experimental results using ten 3D MR patient prostate images showed that the proposed *continuous max-flow algorithm* is capable of providing a robust and efficient segmentation for different prostate zones at the same time, such as PZ, CG and WG, with promising accuracy and reliability. In terms of accuracy,

DSC of $89.2 \pm 4.5\%$ for the whole prostate region(WG), based on the introduced composite intensity appearance model, is better than the result of $86.2 \pm 3.0\%$ obtained by the state-of-art mixture intensity model; DSCs of $68.5 \pm 6.9\%$ and $84.7 \pm 5.2\%$ for PZ and CG yielded by our methods are lower than $75.0 \pm 7.0\%$ and $89.0 \pm 3.0\%$ reported in [14] or $76.0 \pm 6.0\%$ and $87.0 \pm 4.0\%$ reported in [13]. However, these two methods made use of multi-spectral MR information and required manual WG segmentations as initialization. In addition, comparing to these methods, the proposed method also needs less user interactions and computation time. In order to improve the segmentation accuracy, our future studies might put emphasis on incorporating additional prior information, such as texture and shape, or relying on information from multi-spectral MR imaging.

Acknowledgments. The authors are grateful for funding from the Canadian Institutes of Health Research (CIHR) and the Ontario Institute of Cancer Research (OICR). E. Ukwatta acknowledges the support from Natural Sciences and Engineering Research Council (NSERC) Canada Research Scholarship (CGS). A. Fenster holds a Canada Research Chair in Biomedical Engineering, and acknowledges the support of the Canada Research Chair Program.

References

1. Siegel, R., Naishadham, D., Jemal, A.: Cancer statistics, 2012. CA: A Cancer Journal for Clinicians 62(1), 10–29 (2012)
2. Leslie, S., Goh, A., Lewandowski, P.M., Huang, E.Y.H., de Castro Abreu, A.L., Berger, A.K., Ahmadi, H., Jayaratna, I., Shoji, S., Gill, I.S., Ukimura, O.: 2050 contemporary image-guided targeted prostate biopsy better characterizes cancer volume, gleason grade and its 3d location compared to systematic biopsy. The Journal of Urology 187(4, suppl.), e827 (2012)
3. Doyle, S., Feldman, M.D., Tomaszewski, J., Madabhushi, A.: A boosted bayesian multiresolution classifier for prostate cancer detection from digitized needle biopsies. IEEE Trans. Biomed. Engineering 59(5), 1205–1218 (2012)
4. Beyersdorff, D., Winkel, A., Hamm, B., Lenk, S., Loening, S.A., Taupitz, M.: MR imaging-guided prostate biopsy with a closed MR unit at 1.5 T: initial results. Radiology 234(2), 576–581 (2005)
5. Villeirs, G., De Meerleer, G.: Magnetic resonance imaging (mri) anatomy of the prostate and application of mri in radiotherapy planning. European Journal of Radiology 63(3), 361–368 (2007)
6. Haffner, J., Potiron, E., Bouyé, S., Puech, P., Leroy, X., Lemaitre, L., Villers, A.: Peripheral zone prostate cancers: location and intraprostatic patterns of spread at histopathology. The Prostate 69(3), 276–282 (2009)
7. Reinsberg, S., Payne, G., Riches, S., Ashley, S., Brewster, J., Morgan, V., et al.: Combined use of diffusion-weighted mri and 1h mr spectroscopy to increase accuracy in prostate cancer detection. American Journal of Roentgenology 188(1), 91–98 (2007)
8. Kitajima, K., Kaji, Y., Fukabori, Y., Yoshida, K., Suganuma, N., Sugimura, K.: Prostate cancer detection with 3 t mri: Comparison of diffusion-weighted imaging and dynamic contrast-enhanced mri in combination with t2-weighted imaging. Journal of Magnetic Resonance Imaging 31(3), 625–631 (2010)
9. Kirby, R., Gilling, P.: Fast facts: benign prostatic hyperplasia. Health Press Limited (2011)

10. Ghose, S., Oliver, A., Martí, R., Lladó, X., Vilanova, J., Freixenet, J., Mitra, J., Sidibé, D., Meriaudeau, F.: A survey of prostate segmentation methodologies in ultrasound, magnetic resonance and computed tomography images. Computer Methods and Programs in Biomedicine 108(1), 262–287 (2012)
11. Allen, P., Graham, J., Williamson, D., Hutchinson, C.: Differential segmentation of the prostate in mr images using combined 3d shape modelling and voxel classification. In: 3rd IEEE International Symposium on Biomedical Imaging: Nano to Macro, pp. 410–413. IEEE (2006)
12. Yin, Y., Fotin, S., Periaswamy, S., Kunz, J., Haldankar, H., Muradyan, N., Turkbey, B., Choyke, P.: Fully automated 3d prostate central gland segmentation in mr images: a logismos based approach. In: SPIE Medical Imaging, International Society for Optics and Photonics, pp. 83143B–83143B (2012)
13. Makni, N., Iancu, A., Colot, O., Puech, P., Mordon, S., Betrouni, N., et al.: Zonal segmentation of prostate using multispectral magnetic resonance images. Medical Physics 38(11), 6093 (2011)
14. Litjens, G., Debats, O., van de Ven, W., Karssemeijer, N., Huisman, H.: A pattern recognition approach to zonal segmentation of the prostate on MRI. In: Ayache, N., Delingette, H., Golland, P., Mori, K. (eds.) MICCAI 2012, Part II. LNCS, vol. 7511, pp. 413–420. Springer, Heidelberg (2012)
15. Luckhaus, S., Sturzenhecker, T.: Implicit time discretization for the mean curvature flow equation. Calc. Var. Partial Differential Equations 3(2), 253–271 (1995)
16. Boykov, Y., Kolmogorov, V., Cremers, D., Delong, A.: An integral solution to surface evolution PDEs via geo-cuts. In: Leonardis, A., Bischof, H., Pinz, A. (eds.) ECCV 2006. LNCS, vol. 3953, pp. 409–422. Springer, Heidelberg (2006)
17. Yuan, J., Ukwatta, E., Tai, X.C., Fenster, A., Schnoerr, C.: A fast global optimization-based approach to evolving contours with generic shape prior. Technical report CAM-12-38, UCLA (2012)
18. Osher, S., Fedkiw, R.: Level set methods and dynamic implicit surfaces. Applied Mathematical Sciences, vol. 153. Springer, New York (2003)
19. Delong, A., Gorelick, L., Schmidt, F.R., Veksler, O., Boykov, Y.: Interactive segmentation with super-labels. In: Boykov, Y., Kahl, F., Lempitsky, V., Schmidt, F.R. (eds.) EMMCVPR 2011. LNCS, vol. 6819, pp. 147–162. Springer, Heidelberg (2011)
20. Michailovich, O., Rathi, Y., Tannenbaum, A.: Image segmentation using active contours driven by the bhattacharyya gradient flow. IEEE Transactions on Image Processing 16(11), 2787–2801 (2007)
21. Boykov, Y., Veksler, O., Zabih, R.: Fast approximate energy minimization via graph cuts. IEEE Transactions on Pattern Analysis and Machine Intelligence 23, 2001 (2001)
22. Yuan, J., Bae, E., Tai, X.: A study on continuous max-flow and min-cut approaches. In: CVPR 2010 (2010)
23. Yuan, J., Bae, E., Tai, X.-C., Boykov, Y.: A continuous max-flow approach to potts model. In: Daniilidis, K., Maragos, P., Paragios, N. (eds.) ECCV 2010, Part VI. LNCS, vol. 6316, pp. 379–392. Springer, Heidelberg (2010)
24. Bertsekas, D.P.: Nonlinear Programming. Athena Scientific (September 1999)
25. Chambolle, A.: An algorithm for total variation minimization and applications. Journal of Mathematical Imaging and Vision 20(1), 89–97 (2004)
26. Garnier, C., Bellanger, J.J., Wu, K., Shu, H., Costet, N., Mathieu, R., de Crevoisier, R., Coatrieux, J.L.: Prostate segmentation in HIFU therapy. IEEE Trans. Med. Imag. 30(3), 792–803 (2011)
27. Qiu, W., Yuan, J., Ukwatta, E., Tessier, D., Fenster, A.: Rotational-slice-based prostate segmentation using level set with shape constraint for 3D end-firing TRUS guided biopsy. In: Ayache, N., Delingette, H., Golland, P., Mori, K. (eds.) MICCAI 2012, Part I. LNCS, vol. 7510, pp. 537–544. Springer, Heidelberg (2012)